Multimodal imaging reveals multiscale mechanical interplay in vertebral endplate microarchitecture during intervertebral disc loading

Alissa L. Parmenter (1,2,3), Elis Newham (4), Aikta Sharma (1,5), Catherine M. Disney (6), Hans Deyhle (6,7), Federico Bosi (1), Nick J. Terrill (6), Brian K. Bay (8), Andrew A. Pitsillides (5), Himadri S. Gupta (4), Peter D. Lee (1,3)

Corresponding Authors*:* Alissa Parmenter, Peter Lee
Emails: alissa.parmenter.20@ucl.ac.uk
peter.lee@ucl.ac.uk

1. Department of Mechanical Engineering, University College London, UK;
2. Department of Medical Physics and Biomedical Engineering, University College London, UK;
3. Research Complex at Harwell, UK;
4. School of Engineering and Materials Science, Queen Mary University of London, UK;
5. Royal Veterinary College, UK;
6. Diamond Light Source, UK;
7. University of Basel, CH;
8. School of Mechanical, Industrial and Manufacturing Engineering, Oregon State University, USA;

ABSTRACT

The optimal biomechanical function of the spine depends on hierarchical structures spanning the whole joint to molecular scales. The vertebral endplates experience complex, location specific loading from the intervertebral discs, and their biomechanical behaviour is governed by the microarchitecture, mineralisation, and prestrain of their constituent bone and cartilage. Here we use a combination of synchrotron X-ray tomography, digital volume correlation, and wide-angle X-ray diffraction to investigate relationships between microstructure and mechanics, nanoscale mineral structure, and molecular level prestrain in murine vertebral endplates. Our results show radial variation in endplate structure and local mechanical strain, revealing tensile and shear strains as potential drivers of the cartilage to bone transition. Bone contained narrower mineral crystallites under greater compressive prestrain when compared to calcified cartilage. This multiscale structural adaptation supports load resistance adjacent to the annulus fibrosus and elastic deformation below the nucleus pulposus. Our findings reveal the multiscale mechanics of these mineralised tissues, and the methods presented here have the potential to enhance our understanding of biomechanics in health, disease, and aging.

MAIN TEXT

Back pain affects 600 million people worldwide and is the leading cause of years lived with disability (due to increase by 36 % by 2050) [1]. Spine biomechanics plays a critical role in back pain related pathologies such as intervertebral disc (IVD) degeneration[2], osteoarthritis[3], osteoporosis[4], and scoliosis[5]. There is therefore great interest in the biomechanics of the spine and its constituent parts, including the IVDs and vertebral endplates (VEPs)[6], which are highly complex across hierarchical spatial scales (Fig. 1) and experience a large range of movements and mechanical loads in day-to-day life.

The IVD, comprising of the collagenous annulus fibrosus (AF) and proteoglycan rich nucleus pulposus (NP), deforms under loading, applying complex, location specific strains to the calcified VEPs (Fig. 1b). The VEPs support load transfer from the IVD to the vertebral body whilst allowing nutrient transfer and are comprised of calcified cartilage and bone. These mineralised tissues have differing material properties, with the elastic modulus of calcified cartilage an order of magnitude lower than bone[7]; this greater bone stiffness persists even when mineral content is matched to calcified cartilage levels[8] , suggesting that inherent differences in non-mineralised components influences their respective mechanical properties. The formation of different musculoskeletal tissues is thought to be partly driven by the local mechanical environment[9]. Changes in mineralisation and mineralised tissue structure are associated with multiple pathologies, including osteoarthritis [10,11] and IVD calcification[12] .

The murine VEP forms a calcified cartilage epiphysis with distinct secondary ossification centres, separated from the adjacent vertebral bone by a cartilage growth plate[13]. Osteocytes in the bone compartment are considered responsive to prevailing mechanical cues and influence the three-dimensional structure of the VEPs [14,15]. Chondrocytes in cartilage are also mechanosensitive, with changes in their mechanical environment known to also lead to degeneration[16]. VEP injury and degeneration disrupts the mechanical environment, driving IVD degeneration and back pain[17,18], whilst VEP maintenance in health relies on the formation of optimal structures for load absorption

and transfer. An appreciation of how these structures attain their function requires investigation of their biomechanics during the growth stage.

The mechanical function of VEPs is impacted by structures at different spatial scales. At the macroscale, VEP thickness influences their response to load (Fig. 1b). At the microscale, mineralised tissue architecture and tissue mineral density (TMD) dominate (Fig. 1c), with microstructure linked to vertebral failure [19]. At the nanoscale, mineralised collagen fibril structure (Fig. 1d-e) and prestrain impact mechanical properties[20,21]. Prestrain - the inherent strain in a material in its undeformed state - plays a vital mechanical role [2,22,23]; its loss in the AF leads to IVD degeneration [2]. Mineralised tissue prestrain is thought to increase toughness and crack resistance[24,25] , and is partly caused by the contraction of collagen fibrils during the biomineralization process[26,27]. Mineral structure across the VEPs remains unknown and we hypothesise that VEP mineralisation and mineral prestrain enables optimal IVD mechanical function and is partly controlled by load induced strains.

Several techniques can be used to characterise biomechanics at individual spatial scales. Nonetheless, there remains a need for hierarchical, multiscale imaging to bridge the gap between the cell mechanical environment and whole joint biomechanics that can reveal the relationships between mineralised tissue prestrain and whole joint level mechanics.

On the whole joint to microscale, synchrotron X-ray computed tomography (sCT) with digital volume correlation (DVC) is a powerful tool for investigating the strain response of musculoskeletal tissues [28–32], and has been used to measure microscale strains in trabecular bone[31,32]. However, while DVC has been applied to study internal IVD [33,34] and vertebral bone [35] strains, microscale strain patterns in the VEPs have not been examined.

At the nanoscale, wide-angle X-ray diffraction (WAXD) can be used to quantify mineral prestrain[20] and crystallite size[36], and has been used to investigate fracture toughness in bone[37] and dentin[24], as well as how mineral crystal structure changes with osteoarthritis[10]. Mineral crystallites make up 40-

45% of the bone matrix volume, with the degree and nature of collagen mineralisation leading to large changes in tissue mechanical properties[21].

VEP and IVD physiology and pathophysiology thus involves a complex feedback system between structure and mechanical forces across a range of length scales. However, only recently has the technology become available to capture and study aspects of this system via cross-correlative measurements across structural scales. Variation in mineral structure and prestrain across the VEPs has not previously been measured, and the direct correlation between mineral properties and the microarchitecture of mineralised tissues is difficult to observe.

Here we take inspiration from recent correlative studies using sCT and WAXD in other hard tissue systems[37,38], and the development of the Dual Imaging and Diffraction (DIAD) beamline[39] of the Diamond Light Source (DLS) synchrotron, to analyse the structure and biomechanics of murine VEPs across spatial scales. We use synchrotron imaging modalities to investigate whole joint to molecular scale structure and mechanics in intact murine IVDs under physiologically relevant loading. We measure TMD, microarchitecture, and nano-precision local strains to evaluate structure-strain relationships in whole VEPs. Micro-to-nanoscale (Fig. 1c-e) structure and prestrain were measured by spatially correlated sCT and WAXD, to unveil relationships between microarchitecture, TMD, mineral structure and prestrain. These studies yield novel insights in vertebral biology and mineralised tissue biomechanics, underpinning the mechanobiology of IVD function and pathophysiology.

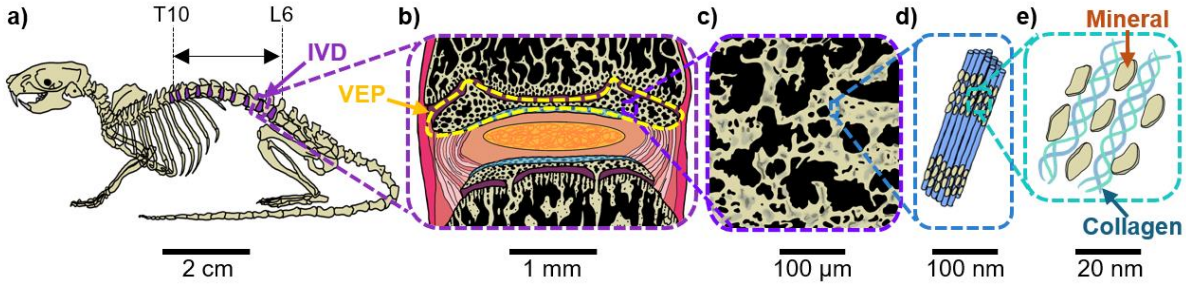

Figure 1 *- **Structural hierarchy in the murine vertebral endplates**. Illustrations of a) the murine skeleton with IVDs investigated in this study, from thoracic vertebra 10 (T10) to lumbar vertebra 6 (L6), shown in purple; b) the murine intervertebral disc, with cranial vertebral endplate outlined in yellow; c) calcified tissue microstructure; d) a mineralised collagen fibril; e) collagen fibres and mineral platelets*

sCT resolves microscale cell-matrix organisation and nano-precision strains by DVC

To achieve microscale resolution of cell-matrix organisation in whole IVDs under physiologically relevant loading conditions, phase contrast sCT scans of 9 murine spine segments under uniaxial compressive load were performed at beamline I13-2 at the DLS synchrotron (Fig. 2a,b). This built on previous work [32,33,40,41] (Methods), optimising experimental parameters to improve image quality whilst reducing scan time and minimising radiation dose. By imaging intact, fresh-frozen, hydrated IVDs under axial compression, the normal function of IVD structures could be observed, whereby the nucleus pulposus (NP) applies hydrostatic pressure in all directions, placing fibres in the AF into tension and causing the endplates to bulge outwards[42] (Fig 2c). Four sCT scans were conducted for each sample; the first under an initial compressive pre-strain of 1 N and the following three under cumulative displacements resulting in bulk IVD strains of 4 %, 8 % and 12 % compression (Fig. 2d). A 1.6 µm voxel size and 4.2 mm x 3.5 mm field of view (FOV) enabled the microstructures of hard and soft tissues to be resolved across the entire IVD (Fig. 2g). This resolution of microscale features allowed the accurate topographical quantification of bone and calcified cartilage microarchitecture across the VEPs using commonly applied metrics (see Methods).

To obtain 3D strain fields across the VEP, sCT datasets were subjected to DVC analysis[29,30], enabling the measurement of nanoscale strains with an order of magnitude improvement in accuracy and precision on previous DVC displacement measurements in whole murine joints [32]. Displacements were measured with an accuracy of 8.2 nm and precision of 6.6 nm, and subsequent Lagrangian strains were calculated from the displacement field with an accuracy of 297 microstrain and precision of 204 microstrain.

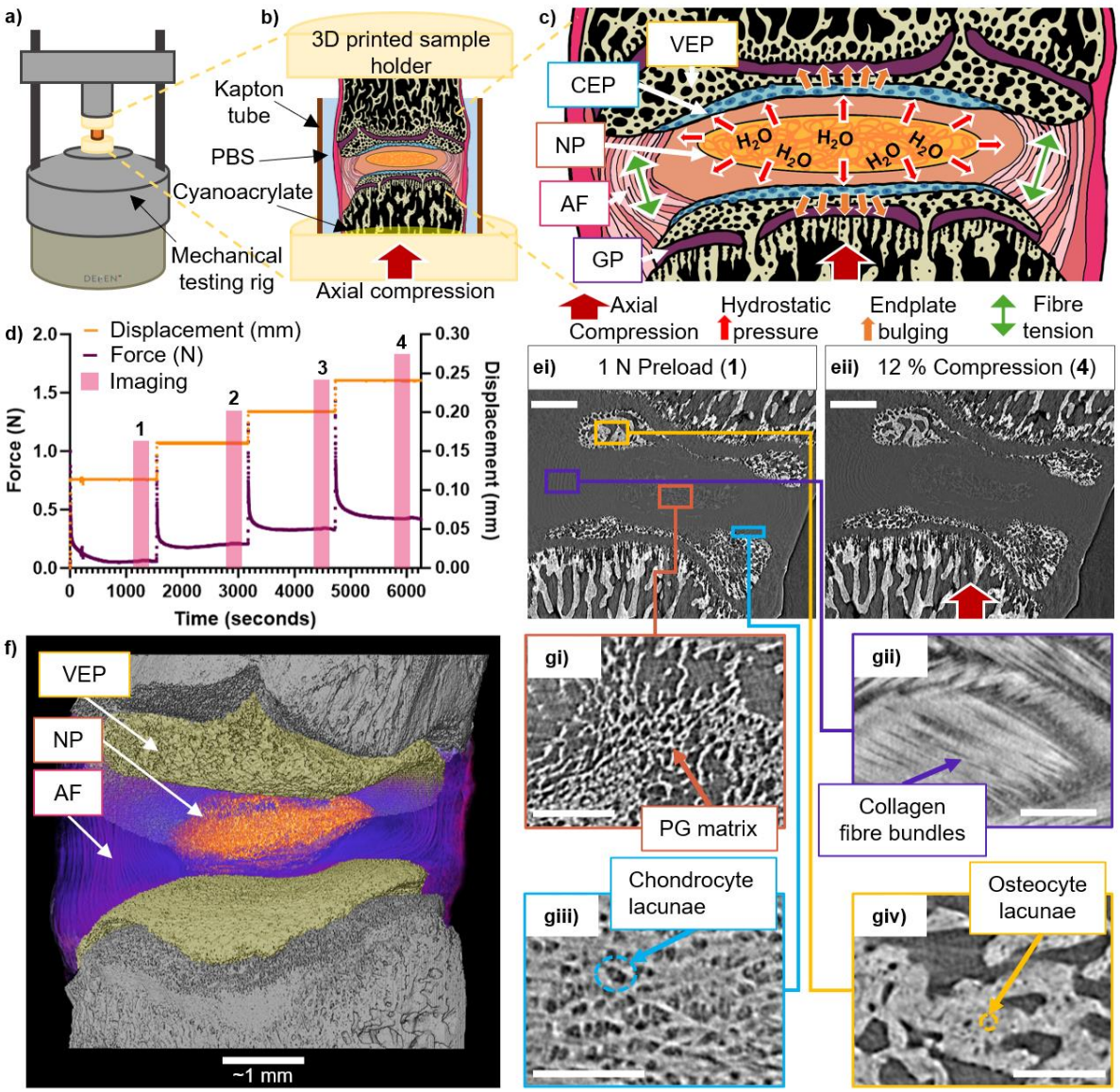

*Figure 2 - **in situ sCT imaging of intact murine intervertebral discs enables visualisation of microscale structure and mechanics across the IVD**. **a)** Schematic of the Deben CT500 mechanical testing rig and custom-built open frame with X-ray translucent carbon pillars to minimise imaging artefacts. **b)** Illustration of a cross-section of the sample environment, with 3D printed sample holder, Kapton tube, phosphate buffered saline (PBS), and cyanoacrylate glue labelled. **c)** Illustration of the IVDs response to axial compression, showing hydrostatic pressure in the nucleus pulposus (NP), fibre tension in the annulus fibrosus (AF), and bulging of the vertebral and cartilage endplates (VEP and CEP respectively) into the growth plate (GP). **d)** Force and displacement readings during one loading experiment, with readings taken during scanning highlighted in pink, scan 1 was taken 20 minutes after application of 1N preload, scan 2 after 4 % compression of the IVD, scan 3 after 8 % compression of the IVD, scan 4 after 12 % compression of the IVD. **e)** Sagittal image slice through a sample under **i)** 1 N preload, corresponding to scan 1 in d, and **ii)** 120 µm compression, corresponding to scan 4 in d, the direction of loading is shown by the red arrow, scalebars represent 0.5 mm. **f)** 3D rendering of a whole IVD sample, with the NP rendered in orange, AF in purple, VEPs in beige, and vertebral bone in grey. **g)** Greyscale images (with varying brightness and contrast settings for visualisation) showing tissue microstructure resolved across all tissues of the IVD, scalebars represent 200 µm **i)** proteoglycan (PG) matrix in the NP, **ii)** collagen fibre bundles in the AF, **iii)** chondrocyte lacunae in the hyaline cartilage endplates, **iv)** osteocyte lacunae in bone.*

Thickening of the peripheral endplate regions enables optimal load transfer from the IVD

To evaluate regional variations in VEP calcified tissue architecture that may modify load transfer from the IVD, sCT and DVC datasets for each endplate (*n* = 16) were subsampled into 10 standardised cubic subvolumes (side length 325 µm) for statistical analysis of structure and strain (Fig. 3a). Repeated measures correlation[43] was used to test for relationships between radial location and microarchitecture, TMD, and local mechanical strain (Fig. 3b). This revealed a decrease in strain with distance from the endplate centre. Central endplate regions across the 16 endplates (Fig. ai region 1) had a mean compressive (3rd principal) strain of 2,104 ± 632 microstrain, mean tensile (1st principal) strain of 1,728 ± 728 microstrain, and mean maximum shear strain of 1,916 ± 619 microstrain. Outer endplate regions (Fig. ai regions 4,7,10) had a mean compressive (3rd principal) strain of 1,316 ± 495 microstrain, mean tensile (1st principal) strain of 1,367 ± 660 microstrain, and mean maximum shear strain of 1,342 ± 498 microstrain. On average, compressive strain in central endplate regions was 788 ± 545 microstrain higher than the outer endplate regions, maximum shear strain was 574 ± 392 microstrain higher, and tensile strain 360 ± 328 microstrain higher after stress relaxation. This increase in local endplate strain below the NP agrees with previous theories that the central endplate region experiences higher strains in vivo [42,44].

Mineralised tissue volume fraction (MV/TV) increased with distance from the endplate centre, corresponding to an increase in thickness of the endplate towards the periphery. The degree of anisotropy was greater towards the outer endplate, potentially due to the highly directional forces applied by the AF. Connectivity to mineralised tissue volume ratio (Con/MV) decreased and septal/trabecular thickness (ST.Th) increased towards the peripheral endplate, indicating a transition from calcified cartilage to bone, which can be distinguished by their resident cellular components visible in our sCT images. In bone, osteocytes reside in lacunae approximately 5 µm in diameter, in agreement with literature[45], which reside in trabeculae 30 – 120 µm in thickness (Fig. 3c). Calcified cartilage contains hypertrophic chondrocytes 20 – 50 µm in size embedded in mineralised lacunae[46], creating a highly porous structure with mineralised cartilage septa 8 – 30 µm in thickness (Fig. 3c).

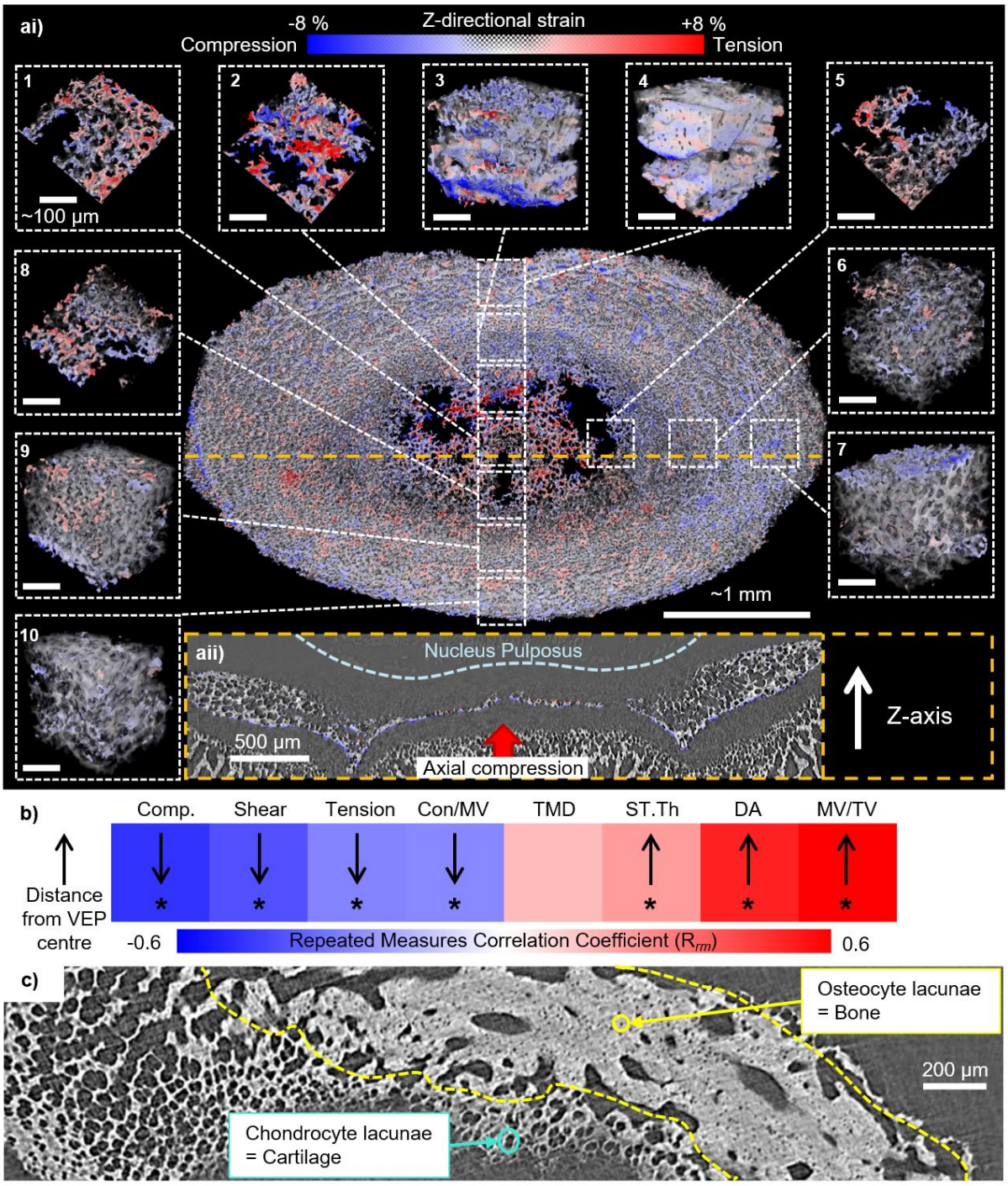

*Figure 3 - **Thickening of the peripheral endplate regions enables optimal load transfer from the IVD**. **ai**) 3D renderings of z-directional strain in a L2-3 cranial endplate. Regions used for statistical analysis are shown in dashed boxes, with scalebars representing ~100 µm; 1 = centre, 2 = anterior inner, 3 = anterior middle, 4 = anterior outer, 5 = lateral inner, 6 = lateral middle, 7 = lateral outer, 8 = posterior inner, 9 = posterior middle, 10 = posterior outer. **aii)** Greyscale image with z-directional strain colourwash showing a slice through the orange dashed line on the 3D rendering in i. **b)** Heatmap of repeated measures correlation coefficient (Rrm) values for mean compressive strain (Comp.), mean maximum shear strain (Shear), connectivity to bone volume ratio (Conn/MV), mean tensile strain (Tension), mean tissue mineral density (TMD), mean septal/trabecular thickness (ST.Th), degree of anisotropy (DA), and mineralised tissue volume fraction (MV/TV), versus distance from the centre of the endplate (distance defined categorically as centre, inner, middle, or outer); downwards arrows represent a negative and upwards arrows a positive correlation; * represents statistical significance at the 5 % level after Holm-Bonferroni correction (see SI for full statistical analysis); c) greyscale cross-section through a VEP showing the microstructures of cartilage and bone, The bone compartment is outlined in yellow and identified by the presence of osteocyte lacunae, whereas the calcified cartilage contains chondrocyte lacunae.*

Spatial mapping of VEP structure to load-induced strain reveals tension and shear as potential drivers of the cartilage to bone transition

To interrogate relationships between microarchitecture, TMD, and local mechanical strain, repeated measures correlation[43] was used to test for links between the mean values for 160 endplate regions across 8 spine segments (Fig. 4a). The generation and quantification of local strain induced by physiologically relevant whole joint loading enables an examination of how the structure of a region contributes to its ability to resist load, and also how the local strains in a region impact the formation of mineralised tissues.

Negative correlations were seen between TMD and local mechanical strain, agreeing with previous studies showing increased stiffness with higher mineralisation[47]. Local mechanical compressive and shear strains negatively correlated with MV/TV, and ST.Th showed positive correlations with local tensile and shear strain.

These correlations reveal two predominant structural types in high strain regions. First, a low TMD calcified cartilage region (identified by the presence of chondrocyte lacunae, Fig. 4biv) with low MV/TV and thin septa found in the central and inner endplate regions adjacent to the NP, which we speculate experiences elastic deformation under loading, leading to high local strains. The second type of high strain region contains trabeculae, high MV/TV, and low Con/MV, indicating that these regions have undergone endochondral ossification to form bone (confirmed by the presence of osteocyte lacunae, Fig. 4biii). Known material properties of bone and calcified cartilage suggest that bony regions should be better at resisting load [7,8]. The high strains measured in these regions therefore implies that the formation of these stronger structures is driven by high tensile and shear strains in vivo. These regions are mostly found in the anterior cranial endplate, and the observation of greater bone volume in this region agrees with computational studies of bone remodelling in human VEPs[15]. These findings provide evidence for long-standing theories that endochondral ossification is inhibited by hydrostatic compressive strain and promoted by octahedral shear strain[9].

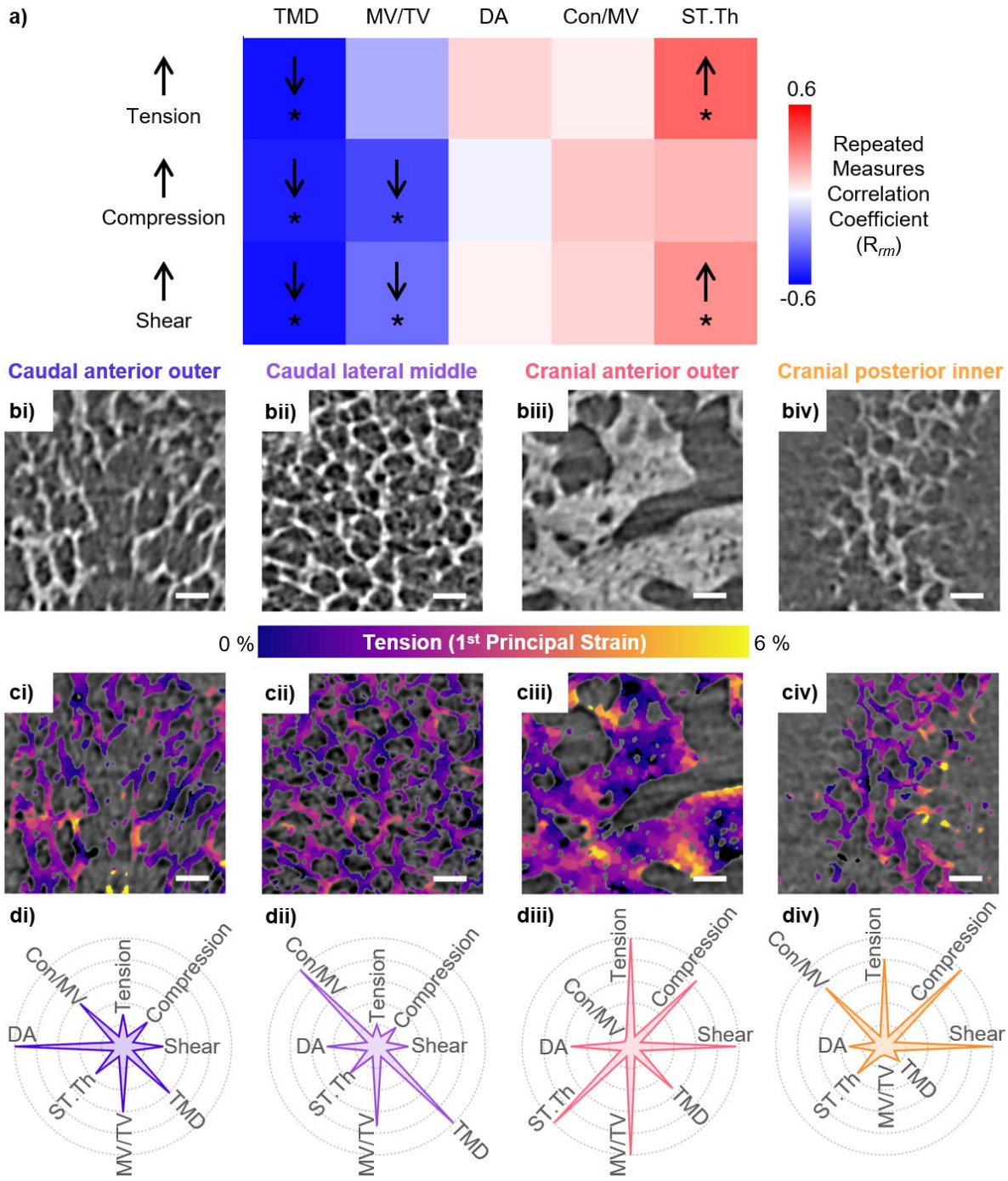

Figure 4 - ***Endplate structure spatially mapped to load-induced strain reveals tension and shear as potential drivers of the cartilage to bone transition****.* ***a****) Heatmap of repeated measures correlation coefficient values for tissue mineral density (TMD), mineralised tissue volume fraction (MV/TV), connectivity to mineralised tissue volume ratio (Con/MV), degree of anisotropy (DA), and mean septal/trabecular thickness (ST.Th) versus tensile strain (Tension), compressive strain (Compression), and maximum shear strain (Shear); * represents statistical significance at the 5 % level after Holm-Bonferroni correction;* ***b)*** *Greyscale image slices,* ***c)*** *tensile strain fields, and* ***d)*** *radar plots of relative strains and structural parameters between 4 regions of a lumbar 4-5 sample:* ***i)*** *the caudal anterior outer,* ***ii)*** *the caudal lateral middle,* ***iii)*** *the cranial anterior outer, and* ***iv)*** *the cranial posterior inner region. Scale bars represent 50 µm.*

Correlative imaging and diffraction enables colocalisation of endplate microarchitecture with nanoscale mineral crystal properties

The character of mineralisation in collagenous tissues is known to influence nanoscale-to-whole joint mechanical properties; however, how the mechanical relationships between nanoscale structure of the mineral phase and its interactions with the organic matrix components determines whole joint function remains unknown. Location and structure of the mineralised crystallites within the collagenous network[10,20,36,48–53] will play a crucial role in this local mechanical equilibrium, and we hypothesise that this differs between calcified cartilage and bone because of inherent differences in their organic components. Because mineral particles are elastic and much stiffer than the organic phase (mineral Youngs Modulus ~100 GPa vs ~1 - 2 GPa for collagen), the stress on the mineral is proportional to the change in lattice spacing (d-period)[20]. Relative changes in d-period in are proportional to the mineral prestrain state and are larger in regions of tensile stress and smaller in regions of compressive stress. Hence, by measuring relative changes in d-period and crystallite structure across the osteochondral junction in the VEP, we will uncover local nanoscale mechanics.

To enable colocalization of microarchitecture in VEP calcified cartilage and bone compartments with these nanoscale mineral crystal properties, consecutive, spatially correlated sCT and WAXD raster scans (Fig. 5a-c) of partial IVDs was performed at the DIAD beamline, DLS [39] (Methods). Physiologically relevant conditions were applied to fresh-frozen quarter IVD segments, with sample hydration and AF native tensile collagen prestrain maintained. Axial and transverse d-periods were derived from the positions of the (002) and (310) peaks respectively (Fig. 5d,e), and mineral crystallite length and width were calculated from the corresponding peak widths[52] (Fig. 5f-g, Methods). Crystallite dimensions were typically between 11.4 ± 1.7 nm (length) and 1.23 ± 0.13 nm (width), consistent with prior results in young, mineralised tissues[50,54].

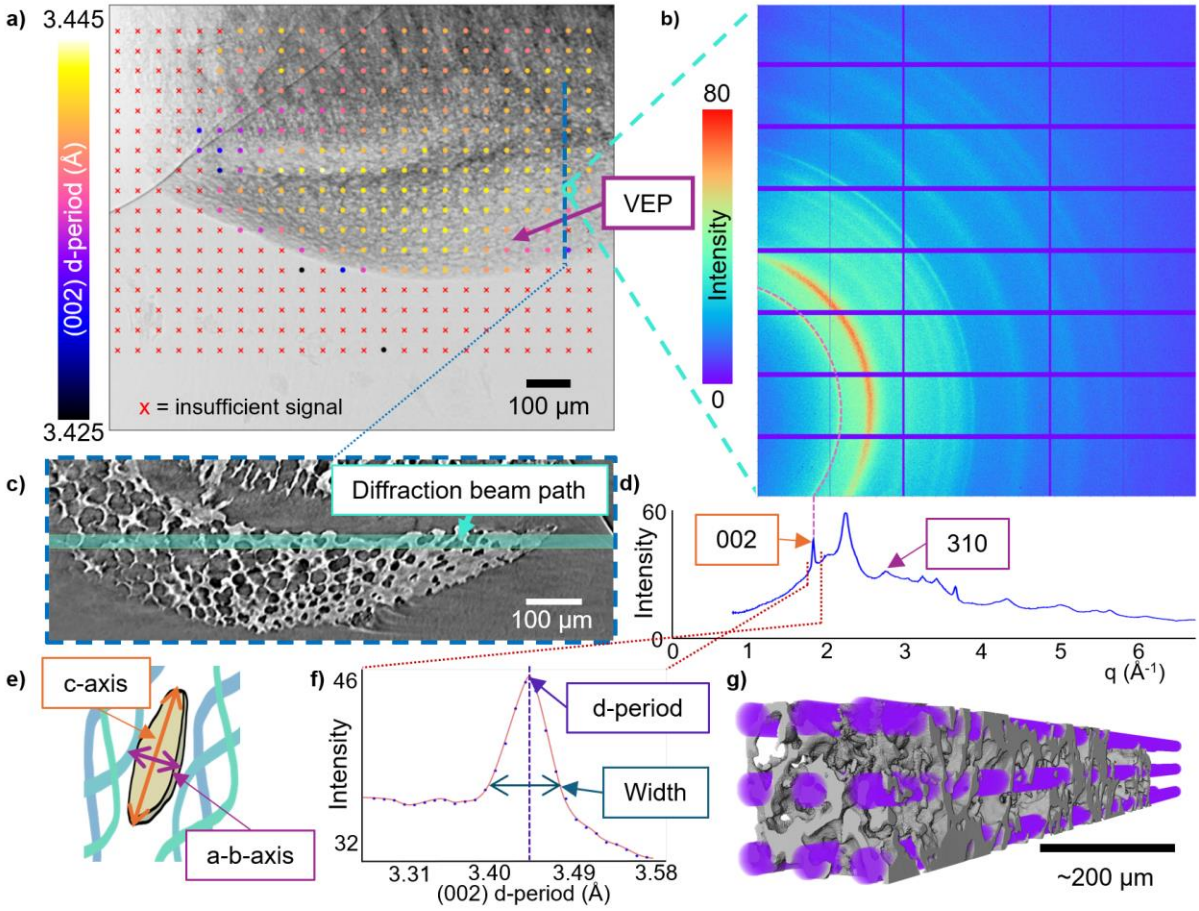

Figure 5 - ***Correlative imaging and diffraction set-up enables colocalization of endplate microarchitecture with nanoscale HAP crystal properties****.* ***a)*** *Map of hydroxyapatite (002) lattice spacing on an X-ray projection of a quarter IVD sample held under tension.* ***b)*** *WAXD intensity pattern from the location highlighted in a), only ~2/3 of the full diffraction rings are visible due to the need to place the WAXD detector off-centre to allow for placement of the imaging camera for sCT (Methods);* ***c)*** *sCT image of the endplate showing the location of the diffraction beam path that produced the WAXD pattern in b), the location of the reconstructed slice is shown as the dashed blue line on the projection in a);* ***d)*** *WAXD pattern in b) integrated over q;* ***e)*** *illustration of a HAP platelet surrounded by collagen, with c and a-b axes labelled;* ***f)*** *HAP (002) peak plotted in d-space, with d-period and width labelled;* ***g)*** *3D rendering of calcified tissue structure (grey) and diffraction beam paths (purple) for one region used for microstructural evaluation and statistical analysis.*

Bone is under greater compressive prestrain and contains narrower crystallites compared to calcified cartilage

New insights into relationships between microscale VEP mineralised tissue architecture and nanoscale crystalline structure/ prestrain were therefore examined by analysing mean values of regions of interest comprising nine WAXD beam paths (Fig. 5g); a total of 194 regions were taken across 8 quarter IVD samples for statistical analysis (Fig. 6a, Methods). This analysis showed that both (002) and (310) prestrain (d-period) in the mineral was higher (more tensile) in regions with greater mineralisation density/ TMD. This aligns with the concept of load sharing between mineral and collagen, and axial fibrillar contraction [53], which we propose leads to greater compressive load on the mineral in regions of lower TMD.

Axial mineral d-period was lower in regions where structural organisation indicates the presence of bone (high MV/TV and ST.Th, low Con/MV, osteocytes present), indicating a greater compressive prestrain in regions that have undergone endochondral ossification (such as the regions shown in Fig. 5bi and iii), and that calcified cartilage is under tensile prestrain relative to bone. This supports the intriguing possibility that the local mechanical equilibrium of the mineral crystallites is functionally distinct between calcified cartilage and bone, possibly due to differences in organic composition.

Mineral crystallite length and width increased with TMD, confirming that more mature mineral has larger crystallites. Crystallite width decreased with ST.Th and increased with Con/MV. This indicates that regions containing bone have narrower crystallites than regions containing calcified cartilage. Positive correlations were seen between (002) d-period and crystallite length ($p < 0.001$), and (002) d-period and crystallite width ($p < 0.001$), implying that longer, wider crystallites are formed when placed under tensile strain along the fibrillar axis, potentially due to greater alignment of gap-overlap channels in the fibril under greater tensile strain.

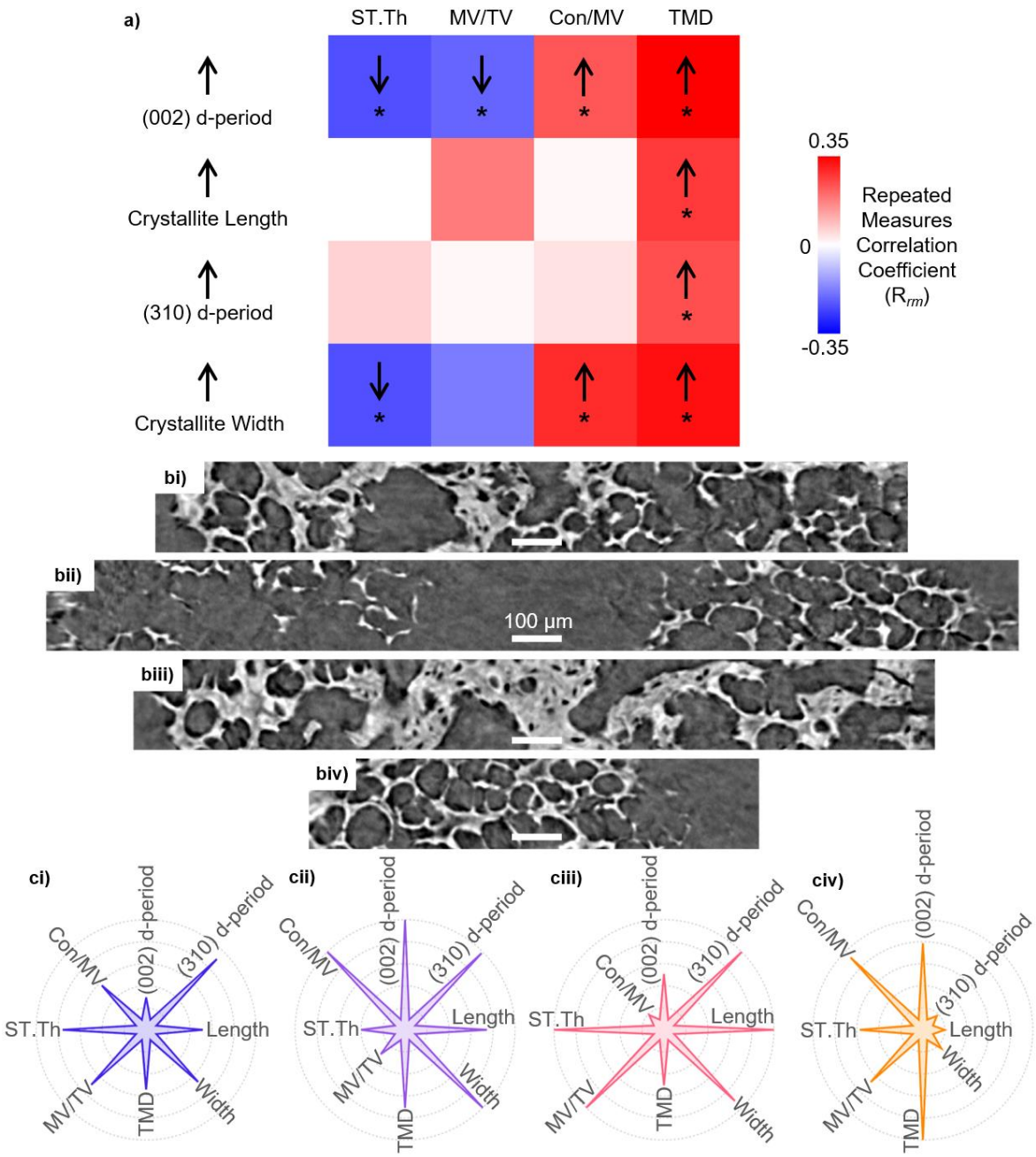

Figure 6 - ***Spatial correlation of sCT and WAXD reveals differences in crystal structure and prestrain between calcified cartilage and bone****.* ***a)*** *Repeated measures correlation coefficient matrix for mean septal/trabecular thickness (ST.Th), mineralised tissue volume fraction (MV/TV), connectivity to mineralised tissue volume ratio (Con/MV), and tissue mineral density (TMD) versus mineral (002) lattice spacing ((002) d-period), mineral crystallite length (Length), mineral (310) lattice spacing (310 d-period), and mineral crystallite width (Width); * represents statistical significance at the 5 % level after Holm-Bonferroni correction.* ***b)*** *Greyscale cross-sections from four VEP regions used for statistical analysis from one sample showing microscale structural variation in the VEP,* ***i)*** *contains a mixture of calcified cartilage and bone,* ***ii)*** *contains sparse calcified cartilage,* ***iii)*** *consists of mostly bone, and* ***iv)*** *contains calcified cartilage, scalebars represent 100 µm.* ***c)*** *Radar charts displaying the relative values of WAXD and sCT based measurements from the four regions shown in b (data used to generate plots given in Supplementary Information).*

DISCUSSION

This study represents a step-change advance in our understanding of the multiscale origins of whole joint biomechanical function, with major implications for the investigation of ageing and degenerative joint diseases such as IVD degeneration and osteoarthritis. The combined analysis of load-induced tissue strains using DVC and molecular-scale mineral prestrain using WAXD, has revealed the important role of mineral prestrain in forming the complex biomechanical pattern underpinning whole VEP joint level mechanics (Fig. 7).

DVC found higher load induced tensile and shear strains in regions containing bone (Fig. 4biii, 7), revealing that local mechanical strain may play a driving role in the cartilage to bone transition, providing crucial evidence for the theory that hydrostatic compression inhibits endochondral ossification[9]. The microscale resolution and nanoscale precision of DVC achieved in this study enables analysis of the local cellular mechanical environment under whole-joint loading, demonstrating the potential of DVC as a tool to bridge the gap between cell mechanobiology and whole joint biomechanics.

WAXD analysis provided nanoscale information on the structure and prestrain state of the mineral component of the extracellular matrix. Regions containing bone (Fig. 6biii, 7) showed greater mineral compressive prestrain which, we hypothesise, both increases VEP toughness in these regions due to mineral compaction, enabling them to resist compression with minimal deformation, and allows for greater levels of tensile strain to be engendered before failure.

In contrast, VEP regions adjacent to the NP (Fig. 4biv) were shown to experience the highest tissue-level compressive strain, agreeing with theories that the endplates bulge under hydrostatic pressure from the NP[42,44]. Our WAXD analysis and quantification of mineralised tissue architectural features in these regions suggest that the mineral is under tensile prestrain relative to the bone regions mentioned previously, which may provide VEP calcified cartilage with a greater level of elastic

compressibility under loading, enabling central endplate bulging to help prevent NP over-pressurisation which would otherwise lead to herniation[44].

This variation in mineral prestrain in calcified cartilage and bone has an interesting correlation with similar findings of higher collagen fibril prestrains (at one step higher in the hierarchical structuring) in calcified cartilage than subchondral bone, measured from small-angle X-ray scattering (SAXS) across bovine metacarpophalangeal joints[23]. These fibrillar differences were interpreted as an adaptation in cartilage allowing for elastic deformation under compression – deforming from an initial relative tensile state to an effective zero load state when compressed. Here, the origin of the lowered mineral prestrain in bone could be explained if the collagen fibril-mineral interface is tighter than in calcified cartilage, leading to greater compressive stress exerted on the mineral platelets by the surrounding collagen (possibly due to a more organised mineral-collagen interrelationship). It has been shown that intrafibrillar mineralisation generates collagen fibrillar contraction, but extrafibrillar mineralisation does not[26] ; in the context of our results, this would imply that bone has more intrafibrillar mineralisation whereas cartilage mineralisation is more extrafibrillar. In this regard, these prestrain differences could also be related to the differing proteoglycan content of bone and cartilage[11,55,56]. Aggrecan, the large aggregating proteoglycan, in cartilage is known to generate a swelling pressure within the tissue, placing collagen fibres under pre-tension, and some remnants of this tensile prestrain may remain in the tissue after mineralisation, resulting in a tensile mineral prestrain in calcified cartilage relative to bone. Here, we have demonstrated using sCT and DVC how these variations in prestrain can be related to whole joint mechanics, furthering the hypothesis that - at the molecular level - relative tensile prestrain in the stiff constituents of the calcified cartilage extracellular matrix enables elastic deformation under macroscale compressive load, whilst compressive prestrain in bone confers resistance to complex loading environments involving tension and shear.

We also observe that regions containing bone have narrower mineral crystallites than calcified cartilage regions (Fig. 7), suggesting differences in mineralisation between these two tissue types. Calcified cartilage contains more extrafibrillar space than bone[54] and contains mostly type II collagen rather than majority type I[23] which may exert a role in the formation of bone apatite[51]. We speculate that the crystallites in mineralised cartilage may be wider due to their extrafibrillar, as opposed to intrafibrillar, bone-like mineralisation[50,57]. Osteoblasts in bone and chondrocytes in cartilage have different directional preferences for the initiation of mineralisation by matrix vesicle secretion[58], and we hypothesise that this may also play a role in the differences in crystallite shape observed in this study. Studies have shown that crystallites with larger aspect ratios increase the stiffness, strength, and toughness of mineralised tissues[59,60], and the wider mineral crystallites in calcified cartilage would have a lower aspect ratio. The variation in prestrain and crystallite shape seen here may explain why bone is stiffer and harder than calcified cartilage even when their mineral content is similar[8], and supports the notion that calcified cartilage acts as an important transition layer in diarthrodial joints, reducing the strains generated at hard-soft tissue boundaries[7,23,54].

CONCLUSIONS

Combined sCT, DVC, and WAXD analyses have enabled whole-joint to nanoscale structural quantification of murine VEPs, showing significant radial variation, transitioning from a thin layer of calcified cartilage centrally adjacent to the NP to thicker peripheral bone structures close to the AF (Fig. 7). Nano-precision DVC enabled quantification of the biomechanics, revealing the presence of higher load-induced strains in the central VEPs adjacent to the NP, which aligns with previous findings[42,44]. Regions containing bone had higher loading-related tissue level tensile and shear strains, potentially demonstrating the instructive role of mechanical loading in the cartilage to bone transition, with complex loading environments involving tension and shear leading to bone formation, and hydrostatic compressive environments remaining as cartilage. Correlative sCT and WAXD exposed differences in mineral prestrain in bone and calcified cartilage, with calcified

cartilage under tensile prestrain relative to the compressive prestrain of bone regions (Fig. 7). Regions containing bone had narrower crystallites compared to calcified cartilage, which likely indicates that cartilage undergoes more extrafibrillar mineralisation. Mineral crystallites were both longer and wider when under relative tensile prestrain. Linking these nanoscale results back to the structure and function of the VEPs, we hypothesise that compressive prestrain and a higher crystallite aspect ratio in the mineral around the peripheral VEPs aids in resisting complex loading from the AF, whereas tensile prestrain and a low crystallite aspect ratio in the calcified cartilage below the NP enables its elastic deformation under hydrostatic compression and prevents NP over-pressurisation.

Our data demonstrate the potential of *in situ* multimodal X-ray probing for multiscale biomechanics and mechanobiology. Each modality offers a unique complementary dataset, allowing a holistic approach to interpreting biomechanics from the whole joint to molecular scales. These techniques have the potential to unravel the biomechanical underpinnings of biomineralization, growth, aging, and the effects of pathologies known to affect mineralised tissue structure, including osteoarthritis and osteoporosis.

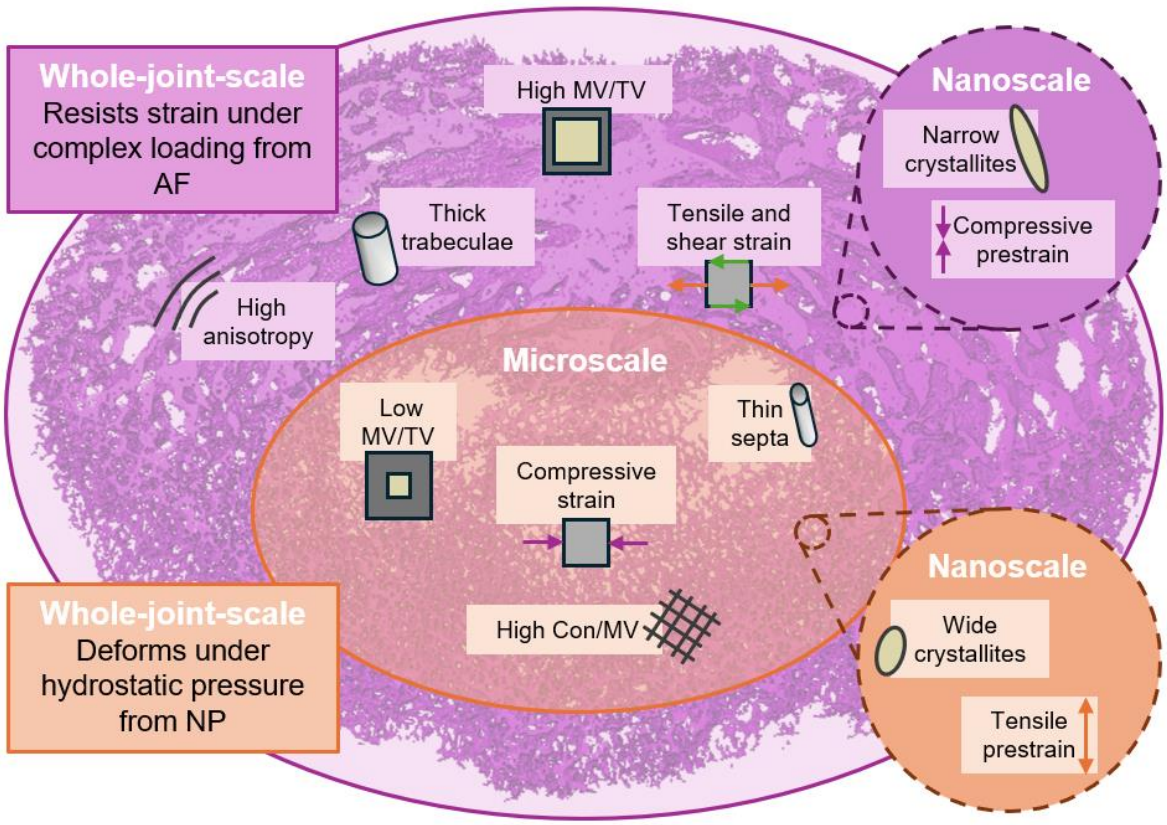

Figure 7 - ***Summary of the differences in loading environment, structure, and prestrain between the central and peripheral vertebral endplates****. At the whole joint scale, the peripheral endplate resists complex loading from the annulus fibrosus (AF); at the microscale the peripheral endplate has high anisotropy, thick trabeculae, high MV/TV (mineralised tissue volume fraction), and experiences high tensile and shear strains; at the nanoscale the peripheral endplate contains narrow mineral crystallites which are under relative compressive prestrain. The central endplate deforms under hydrostatic compressive loading from the nucleus pulposus (NP); at the microscale the central endplate has low MV/TV, thin septa, high Con/MV (connectivity to mineralised tissue volume), and experiences high compressive strains; at the nanoscale the central endplate contains wide mineral crystallites which are under relative tensile prestrain.*

METHODS

Animals and sample preparation

Male 8-week-old Sprague Dawley rats kept in controlled conditions (12:12 hour light:dark cycles, 22 °C and *ad libitum* access to food and water) at the University of Manchester Biomedical Sciences Facility with all tissue collection procedures performed in accordance with the UK Animals (Scientific Procedures) Act 1986, local regulations set by the UK Home Office with institutional approval obtained from the University of Manchester Animal Welfare and Ethics Review Board. Whole spines were dissected and snap frozen in liquid nitrogen prior to storage at -80˚C. Within 24 hours of *in situ* mechanical testing, samples were thawed at room temperature before further dissection.

For *in situ* sCT of whole IVD, individual spinal units (from vertebral levels thoracic 9 to lumbar 6) consisting of an IVD with half vertebrae either side and posterior elements removed. Removal of posterior elements was required to enable visualisation and isolation of the IVD. Dissections were performed using a high precision diamond cutting blade (Accumtom-50; Struers, UK). Sample damage was minimised during dissection through the use of water cooling, a slow feed speed (0.05 mm/s) and 1800 rpm. Spinal level was recorded in terms of vertebral number either side of the IVD for each sample (Sup. Table 4).

For correlative imaging and diffraction experiments, spinal units from spinal levels lumbar 3 to lumbar 6 were further dissected into quarters along the spinal axis, resulting in partial vertebra-annulus-vertebra samples (Sup. Table 5). This was done to ensure samples fit within the smaller imaging field of view at the DIAD beamline (1.38 x 1.16 mm).

In situ mechanical testing

Samples were mounted in a Deben CT500 (Deben, UK) rig containing a 100 N loadcell and custom-built open frame design consisting of an aluminium alloy base cover and two carbon fibre pillars bridged by an aluminium alloy crossbar. The open frame design gave easy access to the samples

during alignment and rehydration and reduced the amount of material in the path of the diffraction beam for dual imaging and diffraction experiments. Custom 3D printed (Acrylonitrile Butadiene Styrene, ABS) sample holders were used for sample mounting.

For in situ sCT of whole IVDs, spinal units were fixed to the bottom 3D printed compression platen using superglue (Vetbond, 3M) and left free at the top. Samples were placed inside polyimide tubing (diameter 6mm, wall thickness 75 µm) filled with phosphate buffered saline (PBS) to maintain sample hydration during scanning. Samples were held under cumulative axial compression, applied in the z-direction from beneath the bottom sample holder during imaging. A 1 N compressive preload was first applied, corresponding to approximately 40 % the animals body weight (260 ± 33 g), designed to prevent over swelling of the nucleus pulposus. The first sCT image was taken 20 minutes after application of the preload to allow for stress relaxation and reduce motion artefacts acquired during scanning. Three further images were taken after applying successive 40 µm displacement steps. 40 µm is equivalent to approximately 4 % the height of a lumbar IVD, therefore successive images were taken at 1 N preload, 4 %, 8 %, and 12 % applied strain respectively. All loads and displacements were applied at a slow rate of 0.1 mm/minute to reduce the amount of stress relaxation after loading.

For correlative imaging and diffraction experiments, partial vertebra-annulus-vertebra samples were fixed at both ends to 3D printed sample holders using superglue (Vetbond, 3M). Samples were placed inside polyimide tubing (diameter 4mm, wall thickness 76 µm) filled with PBS to maintain sample hydration during scanning. A 2.5 N tensile preload was applied before scanning to place annulus fibres into tension and prevent sample motion during scanning. sCT scanning was performed after 30 minutes stress relaxation, followed by WAXD scans.

Phase contrast enhanced sCT imaging of whole IVD

sCT of whole IVDs was performed at the Diamond-Manchester Imaging Branchline I13-2 [61] at Diamond Light Source, UK using a pink beam with mean energy 27.6 keV. Low energy X-rays were

removed using filters (Pyr. Graphite 0.28 mm + 1.06 mm, Al 3.2 mm, Fe 0.14 mm) to reduce radiation dose to the samples. Imaging setup (Sup. Fig. 9) was based on previous experiments [41], with the main changes being a more efficient scintillator, 500 µm LuAG SO14, and larger propagation distance of 0.5 m, allowing shorter exposure times to be used. 1800 projections with 0.1 s exposure time were taken per image volume using fly scanning, resulting in a scan time of 3 minutes and an applied X-ray dose of 29 kG, an 85 % reduction in dose compared to previous experiments [40], see supplementary methods for calculation. Images had a 1.6 µm voxel size and 4.2 mm x 3.5 mm field of view. Limited angle tomography artefacts resulting from the open frame mechanical testing rig were avoided through the use of carbon fibre pillars which were designed to be X-ray transparent, allowing collection of usable tomographic projections at all angles. One pillar covering the field of view results in a 22 % loss of intensity at the detector, and the pillars appear in 19 % of the collected projections (Sup. Fig. 2).

Tomographic datasets were reconstructed using the open-source pipeline Savu[62]. Firstly, projections were pre-processed using flat and dark field correction and lens distortion correction [63], followed by ring artefact removal [64]. Datasets were then reconstructed using the filtered back projection algorithm [65] with Paganin phase retrieval [66] (δ/β value of 100) formatted in 16-bit tif stacks. An unsharp mask (radius = 2.5 pixels and weight = 0.9) was applied to the reconstructed datasets using ImageJ[67] to reduce blurring associated with applying a Paganin filter.

Point cloud generation for DVC

The DVC point cloud specifies the location of the centre of each subvolume used for tracking. Point clouds for the vertebral endplates were created using interactive thresholding and meshing in Avizo 2022.2 (Thermo Fisher Scientific, Waltham, Massachusetts, U.S.). Here, the vertebral endplates are defined as the epiphysis between the vertebra and the IVD. A tetrahedral grid of the mineralised endplate microstructure was created with a minimum distance between nodes of 4.5 voxels (7.3 µm), and the positions of the nodes used to define the point cloud. This resulted in highly dense

point clouds containing ~1 million points per-endplate, resulting in a subvolume overlap of up to 80 %.

Digital Volume Correlation

DVC was performed using the local approach with flexible point cloud specification[29,30]. Source code was supported by CCPi (Collaborative Computational Project in Tomographic Imaging, https://tomographicimaging.github.io/iDVC/, version 21.1.0). All DVC computations were run using spherical subvolumes with 12 degrees of freedom (translation, rotation, and 1st order strain), using a zero-normalised sum-of-square difference function for optimisation. A subvolume diameter of 30 voxels (49 µm) was used with 2000 sampling points per volume. Lagrangian strains were calculated from the displacement field using polynomial fitting and differentiation[30]. A strain window of 25 points was used, resulting in a mean strain window radius of 22 µm, and virtual strain gauge of 92.5 µm.

Accuracy and precision of the displacement and strain fields were calculated using a zero-strain analysis. Standard zero-strain analyses involve using two images taken sequentially of a sample without applying any load. This method can be problematic when imaging highly viscoelastic samples such as the intervertebral disc, as they are likely to have moved between scans, wrongly giving the impression of poor accuracy and precision. An alternative zero-strain method was used for this experiment, where one scan was taken with 3600 projections, which was then split into two sets of 1800 projections to be used for zero strain analysis[40]. This produces two independent scans taken at the same time, removing the potential impacts of viscoelasticity and providing a more robust method of determining true DVC accuracy. Images for zero-strain analysis were reconstructed without projections containing carbon pillars, using ~1600 projections. This was done to prevent differences between the two images caused by the carbon pillars appearing in slightly different locations between the two scans. A point cloud was created for approximately a tenth of the cranial

endplate of the lumbar 1-2 sample used for the zero-strain scans, covering a broad range of microstructures and containing 95,000 measurement points.

Strain accuracy and precision were calculated as the mean absolute error (MAER) and standard deviation of error (SDER) as described by Liu and Morgan [68]

$$MAER = \frac{1}{N}\sum_{k=1}^{N}\left(\frac{1}{6}\sum_{c=1}^{6}\left|\varepsilon_{c,k}\right|\right)$$

$$SDER = \sqrt{\frac{1}{N}\sum_{k=1}^{N}\left(\frac{1}{6}\sum_{c=1}^{6}\left|\varepsilon_{c,k}\right| - MAER\right)^{2}}$$

And analogously for the displacements, where N represents the number of points, k is the point in the point cloud, c is the component of strain, and ε is the strain value. Displacement accuracy ranged from 7.4 nm (x-direction) to 9.6 nm (y direction), with a mean value of 8.2 nm. Displacement precision ranged from 6.0 nm (z-direction) to 7.8 nm (y-direction), with a mean value of 6.6 nm. Strain accuracy ranged from 231 microstrain (xz component) to 383 microstrain (yy component), with a mean value of 297 microstrain. Strain precision ranged from 204 microstrain (xz component) to 329 microstrain (yy component), with a mean value of 264 microstrain (Sup. Fig. 11).

Correlative Imaging and Diffraction

Spatially correlated sCT and WAXD were performed at the DIAD beamline, Diamond Light Source[39] (Sup. Fig. 12). sCT data was acquired using a pink beam filtered with a Pt strip and 4 mm Al to give a mean beam energy of ~ 27 keV. An additional 1.4 mm Al and 0.2 mm Cu were used during sample alignment to reduce X-ray dose on the sample. Sample to detector distance was set to 150 mm. Images were collected using scintillator-coupled optics and a PCO.edge 5.5 camera (Excelitas Technologies, Waltham, MA 02451), with a voxel size of 0.54 µm and a field of view of ~1.38 × 1.16 mm. 2500 projections from 0 to 180˚ with a 50 ms exposure time were collected per scan. 20 dark

and 20 flat field projections were collected for background correction. Images were reconstructed in Savu using filtered back projection, a Fresnel filter, and unsharp mask.

A 17 keV diffraction beam with a 25 µm × 25 µm spot size was used for collection of WAXD data. Data was collected with a PILATUS3X CdTe2M detector (pixel size 172 µm × 172 µm, Dectris AG, Baden-Daetwill, Switzerland) with an angular position (relative to the sample) covering an azimuthal (χ) range of approx. -67° to 27°, and a sample to detector distance of 32.5 cm, determined through calibration with LaB_6 [69]. Diffraction mapping of the endplate was done on a grid of 24 x 17 points with a horizontal step of 54 µm and vertical step of 51 µm, 5 s exposure time was used per point.

WAXD analysis

WAXD data was processed using moving beam azimuthal integration in the DAWN[70] (Version 2.33) software package. Azimuthal range was constrained to -67° to 27°, and radial range between 0.79-7.00 $Å^{-1}$ with a binning value of 1000 (including pixel splitting). Resulting one-dimensional datasets of q versus scattering intensity were analysed using custom designed programs in Python (version 3.10). In each dataset, the (002) peak was isolated by subsampling scattering intensity for q values between 1.75-1.9 $Å^{-1}$. Peaks were modelled by fitting with a Gaussian function using the LMFIT Python library[71], and only points with fitted peak area greater than 5 (in intensity units) recorded. For these models, (002) d-period was estimated from the model centre q_0 along q ($Å^{-1}$) by the equation $d(002) = 2\pi/q_0$; peak height was estimated as the model amplitude; and peak width was taken as 6σ where σ is the width term in the Gaussian function. This same method was repeated for the (310) peak, selecting the q range between 2.63-2.89 $Å^{-1}$ and changing the fitted peak area threshold to greater than 30 intensity units (reflecting the higher absolute intensity values of this scattering region in mineralised tissues). For each WAXD map, nanoscale properties were mapped onto two-dimensional images of sCT reconstructions, summed across their x-axis, using the saved motor positions for each WAXD beampath.

Crystallite length and width were calculated from the 002 and 310 peaks respectively, using the following equation:

$$L = \frac{K\lambda}{B(2\theta)\cos\theta}$$

Where L is the crystallite size, K is a dimensionless shape factor (K = 0.9), λ is the wavelength of the X-ray beam (λ = 0.7348 Å), B is the peak width, and 2θ is the Bragg angle[72].

Regionalised analysis of microstructure, relative TMD, and DVC strain from sCT data

Regions of interest (ROIs) were taken from the sCT datasets for microstructural analysis and quantification of relative TMD. For whole IVD datasets, 200 voxel (325 µm) cubed regions of interest were chosen at 10 anatomical locations in each endplate (see Fig. 3a) across 8 samples, resulting in 160 regions. For correlative imaging and diffraction experiments, ROIs comprising nine diffraction beam paths were used (Fig. 5e), resulting in 125 x 120 µm rectangles projected through the width of the sample. 15-32 regions were taken across 8 samples, resulting in 194 regions for statistical analysis.

Endplate microstructure was binarized using the interactive thresholding module in Avizo, and ROIs were taken using the extract subvolume module. Greyscale images were masked with the binarized calcified tissue microstructure and mean greyscale value for each ROI was calculated as a representative value for tissue mineral density (TMD). There was significant variation in greyscale values between samples, due to differences in the minimum and maximum intensity of X-rays hitting the detector for each sample, which determines the final image histogram; factors that influence this are sample size and the presence of air bubbles. This meant that inter-sample variation in TMD could not be analysed. Binary images were saved as 3D Tiffs and opened in ImageJ for microstructural quantification using BoneJ (BoneJ2 release 7.0.18) [73]. Mineralised tissue volume fraction (MV/TV) was calculated using the Area/Volume fraction module. Osteocyte lacunae were removed from the images using a Maximum followed by a Minimum filter (size = 2.5 voxels for I13 sCT data, size = 8

voxels for DIAD sCT data). Mean septal/ trabecular thickness (ST.Th) was calculated using the Thickness module in BoneJ[74,75] . Degree of anisotropy was calculated using the anisotropy module [76,77] with 2000 directions, 10000 lines, and a sampling increment of 1.73; anisotropy was not analysed for DIAD data due to the inherent anisotropy in the shape of the ROIs analysed. Purify was run on the regions to ensure the presence of a single connected structure before running the connectivity (Modern) plugin[78,79] to calculate the connectivity of the ROIs, this was then divided by mineralised tissue volume to give connectivity to mineralised tissue volume ratio (Con/MV).

Mean values of DVC measured strain were calculated for each ROI in the whole IVD datasets. Tensile strain (Tension) was calculated as the mean 1st principal strain, compressive strain (Compression) was calculated as the magnitude of mean 3rd principal strain, and shear strain (Shear) was calculated as the mean maximum shear strain in the region.

Statistical analysis

Repeated measures correlation was used to determine common intra-sample associations without violating assumptions of independence of observations[43]. The Holm-Bonferroni method was used to deal with familywise error rates[80], and target p-value set to 0.05.

ACKNOWLEDGEMENTS

We thank S. Marussi for his support with the adaptation of the mechanical testing rig. We acknowledge the University of Manchester at Harwell for providing the mechanical testing rig. We thank J. Brunet, J. Liu, S. Rahmani, S. Marathe, J. Chen, and Y. Zhou for their help on beamtimes. We acknowledge funding from Engineering and Physical Sciences Research Council (EP/V011235/1, EP/R513131/1 & EP/V011006/1), Medical Research Council (MR/R025673/1, MR/V033506/1), Royal Academy of Engineering (CiET 1819/10), Chan Zuckerberg Initiative (CZIF2021-006424), Diamond Light Source beamtimes (MG29633-1, SM29784-6). A.L.P. acknowledges support from the i4health Centre for Doctoral Training.

AUTHOR CONTRIBUTIONS

Study conception and experimental design: A.L.P., C.M.D., H.D., N.J.T., B.K.B., A.A.P., H.S.G., P.D.L. **Acquisition of data**: A.L.P., E.N., C.M.D., A.S., H. D., H.S.G. **Data analysis**: A.L.P., E.N. **Drafting of the manuscript**: A.L.P., E.N., A.S., F.B., B.K.B., A.A.P., H.S.G., and P.D.L. **Interpretation of data, revision of the manuscript, final approval and agreement to be accountable for all aspects of the work**: all authors.

COMPETING INTERESTS

The authors declare no competing interests.

DATA AVAILABILITY

All data is available from the corresponding authors upon reasonable request.

REFERENCES

1. Ferreira, M. L. et al. Global, regional, and national burden of low back pain, 1990–2020, its attributable risk factors, and projections to 2050: a systematic analysis of the Global Burden of Disease Study 2021. Lancet Rheumatol 5, (2023).

2. Bonnevie, E. D. et al. Aberrant mechanosensing in injured intervertebral discs as a result of boundary-constraint disruption and residual-strain loss. Nat Biomed Eng 3, (2019).

3. Fine, N. et al. Intervertebral disc degeneration and osteoarthritis: a common molecular disease spectrum. Nature Reviews Rheumatology vol. 19 Preprint at https://doi.org/10.1038/s41584-022-00888-z (2023).

4. Rolvien, T. & Amling, M. Disuse Osteoporosis: Clinical and Mechanistic Insights. Calcified Tissue International vol. 110 Preprint at https://doi.org/10.1007/s00223-021-00836-1 (2022).

5. Aebi, M. The adult scoliosis. European Spine Journal vol. 14 Preprint at https://doi.org/10.1007/s00586-005-1053-9 (2005).

6. Desmoulin, G. T., Pradhan, V. & Milner, T. E. Mechanical Aspects of Intervertebral Disc Injury and Implications on Biomechanics. Spine vol. 45 Preprint at https://doi.org/10.1097/BRS.0000000000003291 (2020).

7. Mente, P. L. & Lewis, J. L. Elastic modulus of calcified cartilage is an order of magnitude less than that of subchondral bone. Journal of Orthopaedic Research 12, (1994).

8. Gupta, H. S. et al. Two different correlations between nanoindentation modulus and mineral content in the bone–cartilage interface. J Struct Biol 149, 138–148 (2005).

9. Carter, D. R., Beaupré, G. S., Giori, N. J. & Helms, J. A. Mechanobiology of skeletal regeneration. in Clinical Orthopaedics and Related Research vol. 355 (1998).

10. Finnilä, M. A. J. et al. Mineral Crystal Thickness in Calcified Cartilage and Subchondral Bone in Healthy and Osteoarthritic Human Knees. Journal of Bone and Mineral Research 37, (2022).

11. Das Gupta, S. et al. Raman microspectroscopic analysis of the tissue-specific composition of the human osteochondral junction in osteoarthritis: A pilot study. Acta Biomater 106, (2020).

12. Zehra, U. et al. Mechanisms and clinical implications of intervertebral disc calcification. Nature Reviews Rheumatology vol. 18 Preprint at https://doi.org/10.1038/s41584-022-00783-7 (2022).

13. Zhang, Y. et al. Histological features of endplates of the mammalian spine: From mice to men. Spine (Phila Pa 1976) 39, (2014).

14. Wang, L., You, X., Zhang, L., Zhang, C. & Zou, W. Mechanical regulation of bone remodeling. Bone Research vol. 10 Preprint at https://doi.org/10.1038/s41413-022-00190-4 (2022).

15. Grosland, N. M. & Goel, V. K. Vertebral endplate morphology follows bone remodeling principles. Spine (Phila Pa 1976) 32, (2007).

16. Hodgkinson, T., Kelly, D. C., Curtin, C. M. & O'Brien, F. J. Mechanosignalling in cartilage: an emerging target for the treatment of osteoarthritis. Nature Reviews Rheumatology vol. 18 Preprint at https://doi.org/10.1038/s41584-021-00724-w (2022).

17. Adams, M. A., Freeman, B. J. C., Morrison, H. P., Nelson, I. W. & Dolan, P. Mechanical Initiation of Intervertebral Disc Degeneration. Spine (Phila Pa 1976) 25, 1625–1636 (2000).

18. Lawan, A., Crites Videman, J. & Battié, M. C. The association between vertebral endplate structural defects and back pain: a systematic review and meta-analysis. European Spine Journal vol. 30 2531–2548 Preprint at https://doi.org/10.1007/s00586-021-06865-6 (2021).

19. Hussein, A. I. & Morgan, E. F. The effect of intravertebral heterogeneity in microstructure on vertebral strength and failure patterns. Osteoporosis International 24, (2013).

20. Gupta, H. S. et al. Cooperative deformation of mineral and collagen in bone at the nanoscale. Proceedings of the National Academy of Sciences 103, 17741–17746 (2006).

21. Ma, C., Du, T., Niu, X. & Fan, Y. Biomechanics and mechanobiology of the bone matrix. Bone Res 10, 59 (2022).

22. Inamdar, S. R. et al. The Secret Life of Collagen: Temporal Changes in Nanoscale Fibrillar Pre-Strain and Molecular Organization during Physiological Loading of Cartilage. ACS Nano 11, (2017).

23. Badar, W. et al. Collagen pre-strain discontinuity at the bone—Cartilage interface. PLoS One 17, e0273832 (2022).

24. Forien, J. B. et al. Compressive Residual Strains in Mineral Nanoparticles as a Possible Origin of Enhanced Crack Resistance in Human Tooth Dentin. Nano Lett 15, (2015).

25. Polishchuk, I. et al. Coherently aligned nanoparticles within a biogenic single crystal: A biological prestressing strategy. Science (1979) 358, (2017).

26. Ping, H. et al. Mineralization generates megapascal contractile stresses in collagen fibrils. Science (1979) 376, (2022).

27. Masic, A. et al. Osmotic pressure induced tensile forces in tendon collagen. Nat Commun 6, (2015).

28. Dall'Ara, E. & Tozzi, G. Digital volume correlation for the characterization of musculoskeletal tissues: Current challenges and future developments. Frontiers in Bioengineering and Biotechnology vol. 10 Preprint at https://doi.org/10.3389/fbioe.2022.1010056 (2022).

29. Bay, B. K., Smith, T. S., Fyhrie, D. P. & Saad, M. Digital volume correlation: Three-dimensional strain mapping using X-ray tomography. Experimental Mechanics 1999 39:3 39, 217–226 (1999).

30. Bay, B. K. Methods and applications of digital volume correlation: http://dx.doi.org/10.1243/03093247JSA436 43, 745–760 (2008).

31. Turunen, M. J. et al. Sub-trabecular strain evolution in human trabecular bone. Sci Rep 10, 13788 (2020).

32. Madi, K. et al. In situ characterization of nanoscale strains in loaded whole joints via synchrotron X-ray tomography. Nat Biomed Eng 4, 343–354 (2020).

33. Disney, C. M. et al. Regional variations in discrete collagen fibre mechanics within intact intervertebral disc resolved using synchrotron computed tomography and digital volume correlation. Acta Biomater 138, 361–374 (2022).

34. Tavana, S. et al. The Effect of Degeneration on Internal Strains and the Mechanism of Failure in Human Intervertebral Discs Analyzed Using Digital Volume Correlation (DVC) and Ultra-High Field MRI. Front Bioeng Biotechnol 8, 1579 (2021).

35. Palanca, M., Cavazzoni, G. & Dall'Ara, E. The role of bone metastases on the mechanical competence of human vertebrae. Bone 173, (2023).

36. Turunen, M. J. et al. Bone mineral crystal size and organization vary across mature rat bone cortex. J Struct Biol 195, (2016).

37. Zimmermann, E. A. et al. Age-related changes in the plasticity and toughness of human cortical bone at multiple length scales. Proceedings of the National Academy of Sciences 108, 14416–14421 (2011).

38. Grünewald, T. A. et al. Bone mineral properties and 3D orientation of human lamellar bone around cement lines and the Haversian system. IUCrJ 10, 189–198 (2023).

39. Reinhard, C. et al. Beamline K11 DIAD: a new instrument for dual imaging and diffraction at Diamond Light Source. urn:issn:1600-5775 28, 1985–1995 (2021).

40. Disney, C. M., Vo, N. T., Bodey, A. J., Bay, B. K. & Lee, P. D. Image quality and scan time optimisation for in situ phase contrast x-ray tomography of the intervertebral disc. J Mech Behav Biomed Mater 138, 105579 (2023).

41. Disney, C. M. et al. Synchrotron tomography of intervertebral disc deformation quantified by digital volume correlation reveals microstructural influence on strain patterns. Acta Biomater 92, 290–304 (2019).

42. Newell, N. et al. Biomechanics of the human intervertebral disc: A review of testing techniques and results. J Mech Behav Biomed Mater 69, 420–434 (2017).

43. Bakdash, J. Z. & Marusich, L. R. Repeated measures correlation. Front Psychol 8, (2017).

44. Curry, W. H. et al. Lumbar spine endplate fractures: Biomechanical evaluation and clinical considerations through experimental induction of injury. Journal of Orthopaedic Research 34, 1084–1091 (2016).

45. Wittig, N. K. et al. Organ and tissue level properties are more sensitive to age than osteocyte lacunar characteristics in rat cortical bone. Bone Rep 4, (2016).

46. Evans, L. A. E. & Pitsillides, A. A. Structural clues to articular calcified cartilage function: A descriptive review of this crucial interface tissue. Journal of Anatomy vol. 241 Preprint at https://doi.org/10.1111/joa.13728 (2022).

47. Currey, J. Incompatible mechanical properties in compact bone. J Theor Biol 231, (2004).

48. Fratzl, P., Fratzl-Zelman, N. & Klaushofer, K. Collagen packing and mineralization. An x-ray scattering investigation of turkey leg tendon. Biophys J 64, (1993).

49. Törnquist, E., Isaksson, H. & Turunen, M. J. Mineralization of cortical bone during maturation and growth in rabbits. J Bone Miner Metab 38, (2020).

50. Fratzl, P., Fratzl-Zelman, N., Klaushofer, K., Vogl, G. & Koller, K. Nucleation and growth of mineral crystals in bone studied by small-angle X-ray scattering. Calcif Tissue Int 48, (1991).

51. Wang, Y. et al. The predominant role of collagen in the nucleation, growth, structure and orientation of bone apatite. Nat Mater 11, (2012).

52. Silva Barreto, I. et al. Multiscale Characterization of Embryonic Long Bone Mineralization in Mice. Advanced Science 7, (2020).

53. Bertinetti, L. et al. Osmotically driven tensile stress in collagen-based mineralized tissues. J Mech Behav Biomed Mater 52, (2015).

54. Zizak, I. et al. Characteristics of mineral particles in the human bone/cartilage interface. J Struct Biol 141, (2003).

55. Lamoureux, F., Baud'huin, M., Duplomb, L., Heymann, D. & Rédini, F. Proteoglycans: Key partners in bone cell biology. BioEssays vol. 29 Preprint at https://doi.org/10.1002/bies.20612 (2007).

56. Poole, A. R. et al. Composition and structure of articular cartilage: A template for tissue repair. in Clinical Orthopaedics and Related Research vol. 391 (2001).

57. Reznikov, N., Bilton, M., Lari, L., Stevens, M. M. & Kröger, R. Fractal-like hierarchical organization of bone begins at the nanoscale. Science (1979) 360, (2018).

58. Anderson, H. C. Molecular biology of matrix vesicles. Clinical Orthopaedics and Related Research vol. 314 Preprint at https://doi.org/10.1097/00003086-199505000-00034 (1995).

59. Alijani, H. & Vaughan, T. J. Exploring the hierarchical structure of lamellar bone and its impact on fracture behaviour: A computational study using a phase field damage model. J Mech Behav Biomed Mater 153, (2024).

60. Jäger, I. & Fratzl, P. Mineralized collagen fibrils: A mechanical model with a staggered arrangement of mineral particles. Biophys J 79, (2000).

61. Rau, C., Wagner, U., Pešić, Z. & De Fanis, A. Coherent imaging at the Diamond beamline I13. physica status solidi (a) 208, 2522–2525 (2011).

62. Atwood, R. C., Bodey, A. J., Price, S. W. T., Basham, M. & Drakopoulos, M. A high-throughput system for high-quality tomographic reconstruction of large datasets at diamond light source. Philosophical Transactions of the Royal Society A: Mathematical, Physical and Engineering Sciences 373, (2015).

63. Vo, N. T., Atwood, R. C. & Drakopoulos, M. Radial lens distortion correction with sub-pixel accuracy for X-ray micro-tomography. Opt Express 23, (2015).

64. Vo, N. T., Atwood, R. C. & Drakopoulos, M. Superior techniques for eliminating ring artifacts in X-ray micro-tomography. Opt Express 26, (2018).

65. van Aarle, W. et al. Fast and flexible X-ray tomography using the ASTRA toolbox. Opt Express 24, (2016).

66. Paganin, D., Mayo, S. C., Gureyev, T. E., Miller, P. R. & Wilkins, S. W. Simultaneous phase and amplitude extraction from a single defocused image of a homogeneous object. J Microsc 206, 33–40 (2002).

67. Schindelin, J. et al. Fiji: An open-source platform for biological-image analysis. Nature Methods vol. 9 Preprint at https://doi.org/10.1038/nmeth.2019 (2012).

68. Liu, L. & Morgan, E. F. Accuracy and precision of digital volume correlation in quantifying displacements and strains in trabecular bone. J Biomech 40, (2007).

69. Besnard, C. et al. The DIAD Approach to Correlative Synchrotron X-ray Imaging and Diffraction Analysis of Human Enamel. Chemical & Biomedical Imaging 2, 222–232 (2024).

70. Basham, M. et al. Data Analysis WorkbeNch (DAWN). J Synchrotron Radiat 22, (2015).

71. Newville, M., Ingargiola, A., Stensitzki, T. & Allen, D. B. LMFIT: Non-Linear Least-Square Minimization and Curve-Fitting for Python. Zenodo (2014).

72. Lange, C. et al. Fetal and postnatal mouse bone tissue contains more calcium than is present in hydroxyapatite. J Struct Biol 176, (2011).

73. Domander, R., Felder, A. A. & Doube, M. BoneJ2 - refactoring established research software. Wellcome Open Res 6, (2021).

74. Dougherty, R. & Kunzelmann, K.-H. Computing Local Thickness of 3D Structures with ImageJ. Microscopy and Microanalysis 13, (2007).

75. Hildebrand, T. & Rüegsegger, P. A new method for the model-independent assessment of thickness in three-dimensional images. J Microsc 185, (1997).

76. Harrigan, T. P. & Mann, R. W. Characterization of microstructural anisotropy in orthotropic materials using a second rank tensor. J Mater Sci 19, (1984).

77. Odgaard, A. Three-dimensional methods for quantification of cancellous bone architecture. Bone vol. 20 Preprint at https://doi.org/10.1016/S8756-3282(97)00007-0 (1997).

78. Toriwaki, J. & Yonekura, T. Euler Number and Connectivity Indexes of a Three Dimensional Digital Picture. Forma 17, (2002).

79. Odgaard, A. & Gundersen, H. J. G. Quantification of connectivity in cancellous bone, with special emphasis on 3-D reconstructions. Bone 14, (1993).

80. Holm, S. A simple sequential rejective method procedure. Scandinavian Journal of Statistics 6, (1979).